Nanoscale

PAPER

View Article Online
View Journal | View Issue

Double-layer CVD graphene as stretchable transparent electrodes†

Cite this: *Nanoscale*, 2014, **6**, 6057

Sejeong Won,‡[a] Yun Hwangbo,‡[b] Seoung-Ki Lee,[c] Kyung-Shik Kim,[b] Kwang-Seop Kim,[b] Seung-Mo Lee,[b] Hak-Joo Lee,[b] Jong-Hyun Ahn,[c] Jae-Hyun Kim*[b] and Soon-Bok Lee*[a]

The stretchability of CVD graphene with a large area is much lower than that of mechanically exfoliated pristine graphene owing to the intrinsic and extrinsic defects induced during its synthesis, etch-out of the catalytic metal, and the transfer processes. This low stretchability is the main obstacle for commercial application of CVD graphene in the field of flexible and stretchable electronics. In this study, artificially layered CVD graphene is suggested as a promising candidate for a stretchable transparent electrode. In contrast to single-layer graphene (SLG), multi-layer graphene has excellent electromechanical stretchability owing to the strain relaxation facilitated by sliding among the graphene layers. Macroscopic and microscopic electromechanical tensile tests were performed to understand the key mechanism for the improved stretchability, and crack generation and evolution were systematically investigated for their dependence on the number of CVD graphene layers during tensile deformation using lateral force microscopy. The stretchability of double-layer graphene (DLG) is much larger than that of SLG and is similar to that of triple-layer graphene (TLG). Considering the transmittance and the cost of transfer, DLG can be regarded as a suitable candidate for stretchable transparent electrodes.

Received 15th January 2014
Accepted 18th March 2014

DOI: 10.1039/c4nr00265b

www.rsc.org/nanoscale

Introduction

Graphene has been regarded as a promising material for stretchable and transparent electrodes owing to its high optical transparency, high mechanical elongation, and high electrical conductivity.[1–7] Considering the fracture strain of pristine graphene obtained by the mechanical exfoliation of graphite, graphene is expected to endure a mechanical strain up to 25% under biaxial deformation.[8] For commercial application of graphene electrodes, graphene should be synthesized by a scalable method such as chemical vapor deposition (CVD)[1,2,7] and should be transferable to a polymeric and transparent film. While CVD graphene with a well-stitched grain boundary (GB) and negligible mechanical damage has a comparable mechanical strength to pristine graphene,[9] macroscopic CVD graphene with a large area statistically contains many overlapped GBs[10] and mechanical damage that originates from its synthesis, etch-out of the catalytic metal, and the transfer processes; thus, its fracture strain is much lower than that of pristine graphene. This critical weakness of CVD graphene is the main obstacle to its commercial utilization for stretchable and transparent electrodes.

Previous reports have demonstrated that CVD graphene on a polymeric substrate has a better mechanical elongation than indium tin oxide (ITO) on the polymeric substrate[1,3,4] and electrically functions up to 6.5% strain under bending and 6% strain under tension.[1–3,11] Multi-layer graphene synthesized on a Ni catalyst was reported to exhibit a linear variation in the electrical resistance up to 1.8% strain, a non-linear variation from 1.8% to 7.1%, and an abrupt increase in the resistance above 7.1%.[12] It should be noted that the synthesized multi-layer graphene has a different interaction among the graphene layers than artificially stacked multi-layer graphene. Artificially stacked multi-layer graphene is fabricated in this study by stacking multiple monolayers of graphene grown on a Cu catalyst, which provides a weaker interaction among the graphene layers than the synthesized multi-layer graphene. In order to quantitatively compare the performance of stretchable conductive thin films, we need to define the electromechanical stretchability under tension as the engineering strain at which the electrical resistance starts to exceed a predefined limit during the electromechanical tension test.[13] The limit value for the electrical resistance should be predetermined depending on the nature of the application in which the stretchable electrodes

[a]*Department of Mechanical Engineering, Korea Advanced Institute of Science and Technology (KAIST), Daejeon, 305-701, Korea. E-mail: sblee@kaist.ac.kr*

[b]*Department of Nanomechanics, Nano-Convergence Mechanical Systems Research Division, Korea Institute of Machinery & Materials (KIMM), 156 Gajungbuk-ro, Yuseong-gu, Daejeon, 305-343, Korea. E-mail: jaehkim@kimm.re.kr*

[c]*School of Electrical & Electronic Engineering, Yonsei University, Sinchon dong, Seodaemoon-gu, Seoul, 120-749, Korea*

† Electronic supplementary information (ESI) available. See DOI: 10.1039/c4nr00265b

‡ These authors equally contributed to this work.

are utilized. As commercial applications in flexible and stretchable electronics are not yet prevalent, there is no limit value that is generally accepted for stretchable electrodes. Considering the electrical resistance data of stretchable electrodes reported by other researchers,[3,11,14] we choose a limit value of 10 in terms of the relative resistance change defined by $\Delta R/R_0$, where ΔR is the difference in the electrical resistance between the deformed and the undeformed states, and R_0 is the electrical resistance in the undeformed state.

In this study, we propose an artificially stacked graphene structure to enhance the stretchability of flexible transparent electrodes. The electromechanical properties of artificially stacked graphene having a different number of layers were characterized using a macroscopic electromechanical tensile tester, and *in situ* AFM tensile tests were independently performed to understand the key mechanism for the improved stretchability of multi-layer graphene fabricated by stacking multiple monolayers of CVD graphene. The behaviors of crack generation and evolution in multi-layer CVD graphene on a polymeric substrate were clearly visualized using lateral force microscopy (LFM) and depended on the number of layers. It was demonstrated that the electromechanical stretchability of double-layer graphene (DLG) is much larger than that of single-layer graphene (SLG) and similar to that of triple-layer graphene (TLG).

Results and discussion

Sample characterization

In order to verify the quality of the prepared samples, we characterized graphene on a polyethylene terephthalate (PET) film using Raman spectroscopy and atomic force microscopy (AFM). Fig. 1a shows the Raman spectra of SLG on a PET film, DLG on a PET film, and the PET film itself. In the figure, the 2D band is clearly identified at around 2690 cm^{-1} in both SLG and DLG, while the G and D bands of graphene overlap with the strong peaks from PET. We transferred our graphene onto a SiO_2/Si substrate to check the quality of our graphene and characterized it with Raman spectroscopy. Fig. S2† shows the Raman spectra of SLG, DLG, and TLG on a SiO_2/Si substrate. The D band (~1350 cm^{-1}) is very weak, and the D-to-G peak intensity ratio range is $0.018 < I_D/I_G < 0.14$.[15] This indicates that our graphene samples are of high quality. In addition, the Raman spectra of DLG and TLG are very similar to those of SLG, but different from those of native multi-layer graphene with Bernal stacking. This is because there is an arbitrary misorientation among the artificially layered graphenes, and thus, the interlayer coupling among the graphene layers is very weak.[16] The measured 2D-to-G-band ratio is presented in Table S1† with respect to the number of layers. The transmittance was measured with an increasing number of graphene layers from one to three, as shown in Fig. S3† and was obtained on the basis of the transmittance of PET. The transmittance gradually decreases with an increasing number of layers, and the absorbance per layer is approximately 2.2%, which is in good agreement with a previous report.[17]

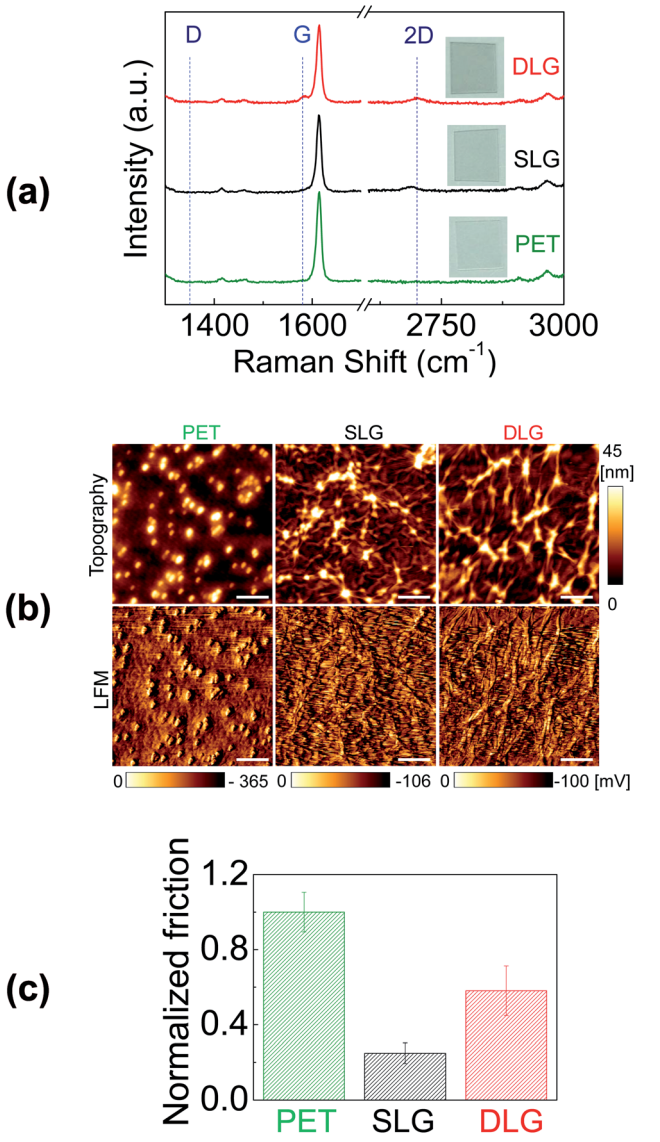

Fig. 1 Characterization of the transferred CVD graphene and the PET substrate. (a) Comparison of the Raman spectra (excitation wavelength $\lambda = 514$ nm) measured from the PET substrate, single-layer graphene on PET, and double-layer graphene on PET. (b) Topography and lateral force microscopy (LFM) images of the PET substrate, single-layer graphene on PET, and double-layer graphene on PET. Scale bar: 1 μm. (c) Normalized friction force of the PET substrate, single-layer graphene on PET, and double-layer graphene on PET.

In addition, AFM was performed in order to identify the surface morphology and friction characteristics of prepared samples. Fig. 1b shows topographic and LFM images of PET, SLG, and DLG. As can be seen in the topography image of PET, a bumpy surface with many peaks and valleys is shown, and its roughness is approximately 6 nm. Many wrinkles are observed from the topography images of SLG and DLG. Figuratively, the graphene layer can be regarded as a handkerchief covering a bumpy ground. LFM images reveal the difference in the frictional properties on the surface. All LFM images in this paper are obtained from backward scans; a bright color means a lower value of friction force, and a dark color indicates a relatively

higher value of friction force. As can be seen in the LFM images, the surface morphology affects the frictional properties. For example, the peaks of PET are observed in the LFM image of PET, and the wrinkles of graphene are observed in the LFM images of SLG and DLG. The frictional force is evaluated by the difference in the lateral force signal between the forward and backward scans,[18] and the normalized friction force in Fig. 1c shows that CVD graphene reduces the friction force of PET significantly. This is consistent with our previous results.[19] It is noted that the friction force of DLG is observed to be larger than that of SLG, contrary to the fact that the friction force on multilayer graphene is lower than that on SLG.[20] Our artificially stacked CVD graphene has a random misorientation among layers, and the adhesion among the stacked graphene layers is relatively lower than that among the graphene layers with Bernal stacking. When the adhesion among graphene layers on a substrate is low, the friction on graphene can increase owing to the puckering effect.[18] Therefore, the increase in friction on DLG can be attributed to the weak adhesion or interaction between artificially stacked CVD graphene layers.

Macroscopic electromechanical tensile-test results

Considering the commercial applications of flexible touch panels and solar cells, graphene on PET (Gr/PET) should be fabricated using a scalable process, and its macroscopic behavior should be characterized. The electromechanical behavior of a Gr/PET electrode was measured using macroscopic specimens with a gauge length of 42 mm, as shown in Fig. 2a, and the electrical resistance throughout the specimen length was measured with respect to the applied strain using the electromechanical tensile-testing system shown in Fig. 2b.

Figure 2c shows the variation in the relative electrical resistance of Gr/PET with a different number of graphene layers. In the figure, a representative data set is displayed to show the typical relationship between the electrical resistance and the strain. The inset shows an enlarged view of the curves when the strain is small. The electromechanical behavior of SLG is much different from that of DLG or TLG, while the behaviors of DLG and TLG are similar to each other. The gauge factors obtained in the strain range from 0 to 0.25% are 2.67, 2.09, and 3.07 in the SLG, DLG, and TLG, respectively, which are in good agreement with those of conventional metallic and graphene strain gauges.[11] The electrical resistance of SLG increases steadily up to 0.6% strain, and the electrical resistance increases rapidly beyond that strain with a slope of 5.34 up to 1.4% strain. When the strain becomes larger than 1.4%, the resistance increases nonlinearly with a reduced slope. The electrical resistance data of DLG and TLG show a similar trend to the data of SLG up to a strain of 0.6%, but surprisingly, they increase steadily beyond that strain with an increase in the strain up to ~30% without any rapid increase in the resistance. The relative resistance change of DLG at a strain of 30% is 13 times less than that of SLG. The electromechanical stretchability of DLG is 36.2%, while that of SLG is only 4.5%. This unexpected behavior of DLG is very beneficial for flexible-touch-panel and solar-cell applications and prompts us to investigate the microscopic mechanism for this unusual stretchability of DLG and TLG. Considering that it is difficult to visualize the damage and cracks in graphene on polymeric substrates using conventional optical and electron microscopy, *in situ* tensile tests under AFM were performed to understand the mechanics of DLG and TLG compared to that of SLG. Because the behavior of TLG is very similar to that of DLG, we focus on DLG and SLG in the rest of this study.

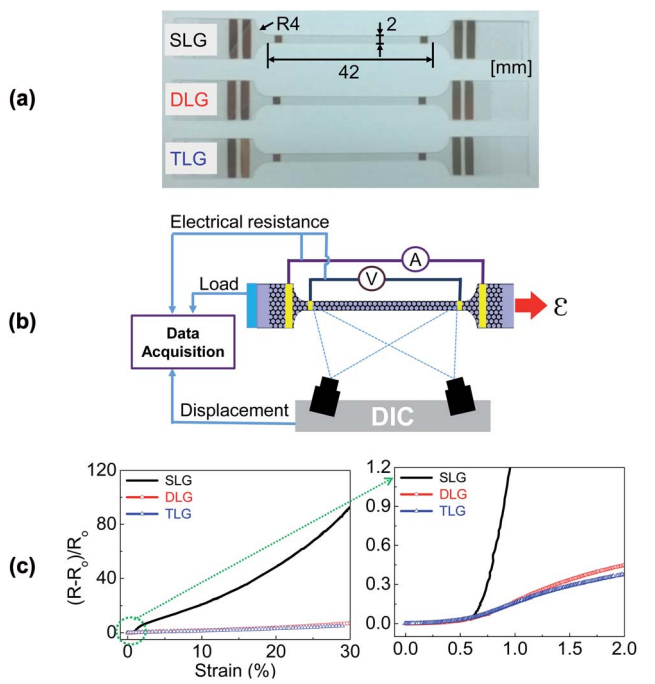

Fig. 2 Electromechanical behavior of single-layer and multi-layer graphene. (a) Photographs of the SLG, DLG, and TLG specimens. (b) Schematic of the electromechanical tensile-testing system. (c) Normalized changes in the electrical resistance of SLG, DLG, and TLG with an applied tensile strain. (SLG: single-layer graphene, DLG: double-layer graphene, and TLG: triple-layer graphene).

Microscopic tensile-test results with *in situ* AFM observation

The *in situ* AFM tensile-testing system shown in Fig. 3a was used to elucidate the factors that primarily contribute to the resistance variation of Gr/PET electrodes under mechanical deformation. Fig. 3b shows the topographies and LFM images for Gr/PET obtained from the *in situ* AFM tensile test with increasing strain. Cracks in SLG are displayed as black lines in the topographies, and these cracks are also visualized as relatively dark lines in the LFM images. The lengths and widths of the dark lines increase as the strain increases. Isolated cracks without any interconnections among them were observed in the topographies of SLG at a strain of 20%, and the average length of the cracks was 4.13 μm (Standard Deviation: 2.79 μm). The cracks in DLG were visualized with poor contrast in the topography images but with better contrast in the LFM images. This is because the difference in the frictional properties between graphene and PET is large, while the height difference induced

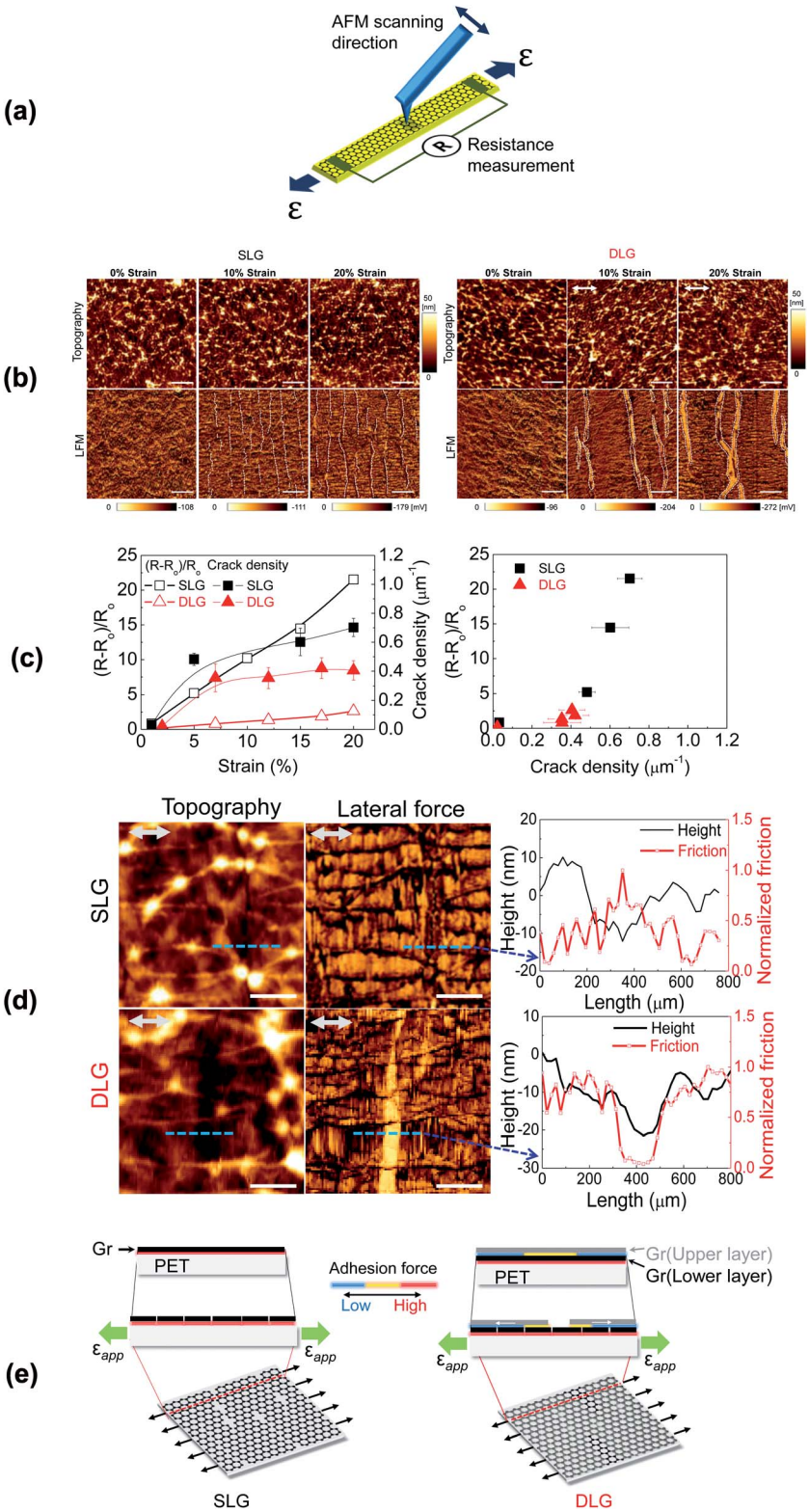

Fig. 3 *In situ* tensile-test–AFM investigation. (a) Schematic of the *in situ* tensile-test–AFM system. (b) Topography and lateral force microscopy (LFM) images of single-layer graphene and double-layer graphene on PET at different strains. Scale bar: 2 μm. (c) Left: normalized electrical resistances and crack densities of single-layer graphene and double-layer graphene on PET according to the strain. Right: normalized electrical resistances according to the crack densities of single-layer graphene and double-layer graphene on PET. (d) Topographies and LFM images of an area with a crack at 20% deformation for single-layer graphene and double-layer graphene on PET. Right side: heights and friction profiles of the blue dotted lines in the topography and LFM images. Scale bar: 500 nm. (e) Electromechanical models of SLG and DLG on PET. Sliding of the upper graphene layer on the lower graphene layer leads to smaller crack density and wider crack width in the upper graphene layer of DLG than in the graphene layer of SLG.

by the thickness of graphene is very small. The cracks in DLG are distributed more sparsely than those in SLG at the same magnitude of strain, while the width of the cracks in DLG is usually much wider than that in SLG. This implies that the applied strain in DLG is released by widening the cracks instead of extending or generating cracks.

It is found that the cracks in graphene are visualized in the LFM images as dark lines for SLG and bright lines for DLG. The variation in the electrical resistance of SLG and DLG is closely related to the crack initiation and growth in graphene as well as dimensional changes in accordance with the applied strain. The crack density was measured from the LFM images of SLG and DLG in order to correlate the resistance variation with the cracks. Five images with an area of 12.5 μm × 12.5 μm were obtained for each value of strain, and the crack density ρ (μm^{-1}) was defined as the total length of surface cracks per unit area[21,22] as

$$\rho = \frac{l_1 + l_2 + \cdots + l_i}{A}$$

where l_i (μm) represents the length of the i^{th} crack in the observed surface area A (μm^2). In the left panel of Fig. 3c, the crack density and the corresponding electrical resistance are plotted in terms of the strain. It is noted that the crack density abruptly increases during the earlier stage of strain for both SLG and DLG, and it slowly increases with a smaller slope when the strain is greater than approximately 7%. The right panel of Fig. 3c shows the relationship between the relative electrical resistance and the crack density. It is found that the electrical resistance increases slowly when the crack density is less than 0.4 μm^{-1}; however, it increases much faster for a larger crack density.

Fig. 3d shows the topography and LFM images of a cracked area at 20% strain for SLG and DLG. The right panels show the height profile and the normalized value of friction along the blue dotted line in the topography and LFM images. For SLG, the cracked region is clearly observed in the topography image, and the corresponding dark line is also observed in the LFM image. The aligned wrinkles are parallel to the tensile direction, and these wrinkles are discontinuous at the crack. As can be seen in the line profiles for the blue dotted lines, the largest value of friction was attained at the crack, and the near-crack area exhibited a relatively larger value of friction than other areas. The value of friction at the crack is about 3.3 times larger than the average value of friction at other areas. This difference is similar to the ratio of friction values for PET to SLG in the graph of Fig. 1c. This indicates that PET is exposed to air along the crack in graphene. While the well-bonded graphene on the substrate has a small value of friction, the detached graphene from the substrate has a large value of friction.[18] The higher value of friction for graphene near the crack indicates that a tiny band of graphene is delaminated from the PET film along the crack.

In contrast to SLG, some wrinkles on DLG are not disconnected by the cracks imaged as bright lines in the LFM images while others are disconnected. The cracks visualized by LFM reside on the upper graphene layer, and the cracks on the lower graphene layer adhered to PET are visualized with poor contrast. The wrinkles on the upper graphene layer of DLG are disconnected by the cracks, but those on the lower graphene layer are not disconnected. The line profile of the blue dotted line in the DLG image indicates a low value of friction at the crack, as represented by the bright line. Considering that the value of friction for SLG is 2.3 times lower than that for DLG, as in Fig. 1c, it is found that the lower graphene layer is exposed around the cracked area of the upper graphene layer of DLG. This also means that the cracks in the upper graphene layer do not overlap with those on the lower graphene layer. The widths of the cracks in DLG become larger with an increase in the strain, while the crack density changes slightly. These observations are attributed to sliding between the upper and lower graphene layers.[23–25] The friction force between the graphene layers approaches zero when the number of layers decreases to two or three,[26] and the interaction force between the upper and the lower layers in the artificially stacked graphene is small compared to multi-layer graphene with Bernal stacking. This enables the upper graphene layer to slide on the lower graphene layer in a DLG specimen, and this sliding releases the external strain transferred to the upper graphene layer from the lower graphene layer on the PET substrate under tension. The critical strain for the onset of interfacial sliding in pristine graphene on the PET structure is reported to be approximately 0.3%,[24] and the sliding between graphene layers can be initiated under a smaller value of strain due to the small interaction and friction between them. In addition, we have also conducted XRD measurements to confirm the stack disorder of graphene layers, which can further prove the existence of interlayer sliding among the graphene layers as shown in Fig. S4.† However, it was found that the XRD peaks of the PET substrate were dominant in our samples and we could not obtain any useful information from XRD measurements. This is probably because the graphene layers are too thin to be measured by XRD, which implies that the tensile testing method with *in situ* AFM observation, as proposed in this study, can be the most effective way for investigating the electromechanical behavior of ultra-thin materials such as graphene.

From the results of the above AFM investigation, electro-mechanical models of SLG and DLG are constructed and presented in Fig. 3e. For SLG, the tensile strain applied to the PET substrate is transmitted with a small loss to the graphene layer owing to the good adhesion between graphene and PET. Even for a strain of 0.6%, the electrical resistance of SLG begins to rapidly increase, meaning that cracks can propagate or be generated at this small strain. In contrast, the strain applied to the PET substrate for DLG is transmitted to the lower graphene layer bonded to the PET substrate; however, the lower graphene layer transmits the strain with a large loss to the upper graphene layer owing to the small interaction between the two layers. The difference in the strain between the two layers results in interlayer sliding and consequently leads to a different crack density between SLG and the upper graphene layer of DLG. A smaller crack density in DLG is responsible for the higher stretchability of DLG than SLG. Our results show that cracks are often generated at a strain smaller than the failure

strain reported in other studies.[8,9,20] The reason can be attributed to intrinsic defects in macroscopic CVD graphene and extrinsic damage in the graphene transferred to PET during the Cu-etching and transfer processes. Because cracks are easily generated at very small strains in CVD graphene, we need to check its reliability under repeated loading.

Cyclic-loading test results

For reliable operation of a graphene electrode during the lifetime of a product, the electrical conductivity is a basic property that should be preserved under repeated mechanical loading. Here, we performed simple loading and unloading tests to verify the reliability of Gr/PET electrodes with a different number of layers under cyclic loading. The loading and unloading of Gr/PET specimens were repeated with an increasing amount of strain using the tester shown in Fig. 2b, and the normalized resistance variation is shown with respect to the applied tensile strain in Fig. 4a. The stress–strain curve of DLG on PET is shown in the inset of Fig. 4a and is identical to that of bare PET or SLG on PET. This indicates that the mechanical behavior of the graphene electrode is dominated by that of PET because the thickness of graphene is negligible compared to that of PET. The hysteresis and recovery behaviors due to the viscoelastic properties of PET are clearly observed and are closely related to the electromechanical behavior of the graphene layer on PET, as will be discussed later. Fig. 4a shows a large difference in the variation of the electrical resistance between SLG and DLG after several loading and unloading cycles. For DLG, the electrical resistance increases gradually during loading and returns along the same curve during unloading when the strain is less than 1%. For a larger strain, *e.g.*, 1.5%, the unloading curve deviates from the initial loading curve, but the reloading curve is very similar to the unloading curve after the unloading period. Interestingly, the electrical resistance for the reloading period is a little smaller than that for unloading at the same tensile strain, and this can be attributed to the viscoelastic recovery of PET. Even for the loading and unloading tests between 0.5% and 5% strain, the resistance curves are very stable and coincident for the loading and unloading periods. The fact that the two curves for the loading and unloading periods are coincident indicates that the crack density in graphene is preserved during those periods. Similarly, the fact that the two curves deviate from each other indicates that the crack density changes. For SLG, the electrical resistance curves for loading and unloading are similar to each other when the strain is less than 0.5%. For a larger strain, however, the resistance increases with a much larger slope than that of DLG during the loading period, and the resistance curves for the loading and unloading curves become unstable, even for the strain range from 0.1% to 1.5%. From the above discussion, it is noted that the crack density during the loading and unloading periods is preserved for DLG up to a strain of 5%, while it becomes unstable for SLG, even below a strain of 1.5%. For verifying the repeated usage of DLG, electromechanical fatigue tests were performed for a controlled total strain at a frequency of 0.2 Hz. A mean strain of 4.85% was chosen as the largest strain as shown in Fig. 4a, and the strain amplitude was chosen as 0.95% considering the elastic region of the PET substrate. Fig. 4b shows the normalized electrical resistance variation of SLG and DLG with respect to the number of loading cycles. While the electrical resistance of SLG on PET abruptly increases at approximately 2800 cycles, that of DLG on PET is very stable up to the maximum number of tested cycles of 7500.

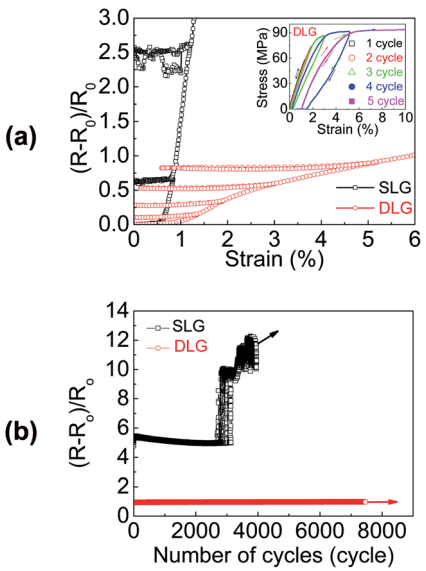

Fig. 4 Electromechanical responses of single-layer and double-layer graphene under a simple loading and unloading test. (a) Variation of the normalized electrical resistance of single-layer and double-layer graphene on PET under a simple loading and unloading test. The inset is the corresponding strain–stress curve of double-layer graphene on PET. (b) Variation of the normalized electrical resistance of SLG and DLG on PET under cyclic loading. The stability of the electrical resistance is investigated.

Conclusions

This work presents an artificially stacked CVD graphene structure as a promising solution for stretchable transparent electrodes. While SLG on PET suffers from a low stretchability of 4.5% resulting from intrinsic defects and extrinsic damage, DLG on PET exhibits a superior stretchability of 36.2% owing to the strain relaxation facilitated by the sliding of the upper graphene layer over the lower one attached to PET. The macroscopic differences in the electromechanical behaviors among SLG, DLG, and TLG were characterized with a tensile tester equipped with real-time electrical resistance and optical strain measurement units, and the higher stretchability of multi-layer graphene on a PET substrate was demonstrated compared to SLG on PET. Using an *in situ* micro-tensile tester equipped with an AFM and an electrical resistance measurement unit, the crack distributions developed in the graphene electrodes were visualized during tensile tests. The microscopic mechanics for the enhanced stretchability of DLG was found to be the interlayer sliding resulting from the weak interaction between the two artificially stacked graphene layers. This study provides a straightforward method and understanding of the mechanics for solving the low-stretchability problem of CVD graphene and

can accelerate the widespread utilization of CVD graphene for flexible, stretchable, and wearable electronics.

Experimental section

Growth and transfer of graphene onto a PET substrate

As illustrated in Fig. S1,† multi-layer graphene was formed by a direct layer-by-layer transfer method to reduce the polymethylmethacrylate (PMMA) residue that affects the mechanical properties of graphene. First, a monolayer graphene film was synthesized in a quartz tube reaction chamber placed in a furnace using 25 μm-thick Cu foil as a catalytic substrate. The Cu foil was loaded into the quartz tube and preheated at 1000 °C for 2 h 40 min with H_2 (H_2 = 10 sccm at 98 mTorr) in order to eliminate the copper oxide on the surface of the substrate to anneal the Cu foil. A CH_4–H_2 gas mixture (1 sccm and 10 sccm, respectively, at 130 mTorr) was introduced into the quartz tube for 5 h 30 min while maintaining the temperature at 1000 °C, and the furnace was then cooled down to room temperature with only H_2 (H_2 = 10 sccm at 100 mTorr). After growth, the copper substrate was etched using a 0.1 M ammonium persulfate solution to separate graphene from the copper foil. In this process, PMMA was used as a supporting layer to hold the graphene stably because graphene can be damaged by the wet-etching process. PMMA-coated graphene was rinsed with DI water for 30 min and transferred onto the graphene grown on the copper foil, realizing a PMMA-covered double layer of graphene on the copper foil without any residue between the graphene layers. The PMMA-free interface between graphene layers is very critical in this study. After the synthesis of graphene, we fabricated graphene layers on a PET substrate using the direct-transfer method illustrated in Fig. S1.† Although various polymers have been studied as possible substrates for electronic devices, PET substrates are widely used for display applications because of their superior optical properties.[27] Regarding the direct-transfer process used in this study, it is possible to ensure that no PMMA residue exists between the graphene layers because a layer of graphene is transferred directly onto another graphene layer grown on Cu foil. From this technique, we could successfully fabricate DLG on PET and TLG on PET without any contamination between the graphene layers. The sheet resistances of SLG, DLG, and TLG on PET were 679, 372, and 365 Ohm per sq., respectively. The polymer substrate used in this study was a 188-μm-thick PET film coated with a primer on one side to improve adhesion.

Macroscopic electromechanical tensile test

In order to obtain the electromechanical properties of graphene with macroscopic dimensions depending on the number of graphene layers, a sheet of multi-layer graphene on a PET film was cut into a dog-bone shape with a gauge length of 42 mm and a width of 2 mm using a cutting plotter (Graphtec FC8000, Graphtec America, Inc.), as shown in Fig. 2a. This shape was designed according to ASTM D882-09 and ISO527-3, which are standard test methods for the tensile properties of a thin plastic sheet. Au (200 nm)/Ti (3 nm) films were deposited on Gr/PET using a shadow mask for the electrode to measure the electrical resistance. A Ti film was used to increase the adhesion between the Au thin film and the graphene layer. Fig. 2b shows a schematic of the electromechanical tensile-testing system. A commercial tensile tester was utilized (Tytron 250, MTS, Inc.), and the strain rate for the test was 0.0004 s^{-1}. A non-contact digital image correlation (DIC) method (Aramis 4M, GOM Co., Ltd) was used for the precise measurement of strain, and this improved the accuracy of our experimental results, while others have used the grip-to-grip distance for measuring strain, which suffers from uncertainty caused by slippage at the grips. The strain resolution of this equipment was 100 με. A current source meter (Keithley 2400 Source Meter, Keithley Instruments, Inc.) and a multimeter with high accuracy (2812A Nanovoltmeter, Keithley Instruments, Inc.) were used to measure the small variation in the electrical resistance during the tensile test. In addition, we minimized the effects of contact resistance between the lead wire and the specimen using the four-wire method. The electrical resistance was obtained by measuring the voltage drop of the specimen at a current of 1 μA, and this small current was chosen to prevent the sample from being heated.

Microscopic electromechanical tensile test with *in situ* observation by AFM

The microscopic behavior of graphene under tensile strain was observed *in situ* using AFM. For the *in situ* AFM tensile test, we combined a tiny tensile tester (Microtest, Deben UK, Ltd) with an AFM (JPK Co., tapping mode) with specially designed assembling parts and electrical measurement units. Fig. 3a shows a schematic of the *in situ* AFM tensile-testing system developed in this study, and AFM images were obtained in contact mode for several applied tensile strains. Typically, the topographic images provided us with less contrast for the cracks and defects than the LFM images. On the basis of the crack generation and evolution revealed by LFM, the mechanics of the enhanced stretchability of multi-layer graphene was analyzed.

Acknowledgements

This research was supported by the Industrial Core Technology Development Programs of the Korean Ministry of Knowledge Economy (grant 10033309), the National Platform Technology Programs of the Korean Ministry of Knowledge Economy (grant 10034751), and the Development Program of Manufacturing Technology for Flexible Electronics (SC0970) of the Korea Institute of Machinery and Materials.

References

1 S. Bae, H. Kim, Y. Lee, X. Xu, J.-S. Park, Y. Zheng, J. Balakrishnan, T. Lei, H. R. Kim, Y. I. Song, Y. J. Kim, K. S. Kim, B. Őzyilmaz, J. H. Ahn, B. H. Hong and S. Iijima, *Nat. Nanotechnol.*, 2010, **5**, 574–578.

2 K. S. Kim, Y. Zhao, H. Jang, S. Y. Lee, J. M. Kim, K. S. Kim, J.-H. Ahn, P. Kim, J.-Y. Choi and B. H. Hong, *Nature*, 2009, **457**, 706–710.
3 S.-K. Lee, B. J. Kim, H. Jang, S. C. Yoon, C. Lee, B. H. Hong, J. A. Rogers, J. H. Cho and J.-H. Ahn, *Nano Lett.*, 2011, **11**, 4642–4646.
4 L. Gomez De Arco, Y. Zhang, C. W. Schlenker, K. Ryu, M. E. Thompson and C. Zhou, *ACS Nano*, 2010, **4**, 2865–2873.
5 S. Lee, K. Lee, C.-H. Liu and Z. Zhong, *Nanoscale*, 2012, **4**, 639–644.
6 S. Bae, S. J. Kim, D. Shin, J.-H. Ahnand and B. H. Hong, *Phys. Scr.*, 2012, **T146**, 014024.
7 X. Li, W. Cai, J. An, S. Kim, J. Nah, D. Yang, R. Piner, A. Velamakanni, I. Jung, E. Tutuc, S. K. Banerjee, L. Colombo and R. S. Ruoff, *Science*, 2009, **324**, 1312–1314.
8 C. Lee, X. Wei, J. W. Kysar and J. Hone, *Science*, 2008, **321**, 385–388.
9 G.-H. Lee, R. C. Cooper, S. J. An, S. Lee, A. van der Zande, N. Petrone, A. G. Hammerberg, C. Lee, B. Crawford, W. Oliver, J. W. Kysar and J. Hone, *Science*, 2013, **340**, 1073–1076.
10 A. W. Tsen, L. Brown, M. P. Levendorf, F. Ghahari, P. Y. Huang, R. W. Havener, C. S. Ruiz-Vargas, D. A. Muller, P. Kim and J. Park, *Science*, 2012, **336**, 1143–1146.
11 V. P. Verma, S. Das, I. Lahiri and W. Choi, *Appl. Phys. Lett.*, 2010, **96**, 203108.
12 S.-H. Bae, Y. Lee, B. K. Sharma, H.-J. Lee, J.-H. Kim and J.-H. Ahn, *Carbon*, 2013, **51**, 236–242.
13 *Semiconductor devices – Micro-electromechanical devices – Part 22: Electromechanical tensile test method for conductive thin films on flexible substrates*, International Electrotechnical Commission (IEC) Standard 62047–22, 2014.
14 X. Li, R. Zhang, W. Yu, K. Wang, J. Wei, D. Wu, A. Cao, Z. Li, Y. Cheng, Q. Zheng, R. S. Ruoff and H. Zhu, *Sci. Rep.*, 2012, **2**, 870.
15 L. M. Malard, M. A. Pimenta, G. Dresselhaus and M. S. Dresselhaus, *Phys. Rep.*, 2009, **473**, 51–87.
16 J. Hass, F. Varchon, J. Millán-Otoya, M. Sprinkle, N. Sharma, W. A. de Heer, C. Berger, P. N. First, L. Magaud and E. H. Conrad, *Phys. Rev. Lett.*, 2008, **100**, 125504.
17 R. R. Nair, P. Blake, A. N. Grigorenko, K. S. Novoselov, T. J. Booth, T. Stauber, N. M. R. Peres and A. K. Geim, *Science*, 2008, **320**, 1308.
18 Q. Li, C. Lee, R. W. Carpick and J. Hone, *Phys. Status Solidi*, 2010, **247**, 2909–2914.
19 K.-S. Kim, H.-J. Lee, C. Lee, S.-K. Lee, H. Jang, J.-H. Ahn, J.-H. Kim and H.-J. Lee, *ACS Nano*, 2011, **5**, 5107–5114.
20 C. Lee, X. Wei, Q. Li, R. Carpick, J. W. Kysar and J. Hone, *Phys. Status Solidi*, 2009, **246**, 2562–2567.
21 R. M. Niu, G. Liu, C. Wang, G. Zhang, X. D. Ding and J. Sun, *Appl. Phys. Lett.*, 2007, **90**, 161907.
22 X. F. Zhu, B. Zhang, J. Gao and G. P. Zhang, *Scr. Mater.*, 2009, **60**, 178–181.
23 L. Xu, T.-B. Ma, Y.-Z. Hu and H. Wang, *Carbon*, 2012, **50**, 1025–1032.
24 T. Jiang, R. Huang and Y. Zhu, *Adv. Funct. Mater.*, 2014, **24**, 396–402.
25 S.-I. Park, J.-H. Ahn, X. Feng, S. Wang, Y. Huang and J. A. Rogers, *Adv. Funct. Mater.*, 2008, **18**, 2673–2684.
26 L. Xu, T.-B. Ma, Y.-Z. Hu and H. Wang, *Nanotechnology*, 2011, **22**, 285708.
27 J. Jang, *Mater. Today*, 2006, **9**, 46–52.